Electronic Journal of Structural Engineering

Original Article

Cite this: DOI:10.56748/ejse.24673

Received Date: 13 August 2024
Accepted Date: 12 December 2024

1443-9255
https://ejsei.com/ejse

Experimental study of the seismic performance of pile groups with integrated building - bridge structure in liquefiable soils: A case study

Chao KONG[a*], Hailing XU[b], Dong LIN[b], Wenteng PAN[b], Guang HUANG[a]
[a] School of Civil Engineering and Architecture, Southwest University of Science and Technology, Mianyang, 621010, China
[b] China Railway Fourth Bureau Group First Engineering Co., Ltd, Hefei 621024, China
*Corresponding author: kongchao@swust.edu.cn

Abstract

The integrated building-bridge structure system represents integrated railway stations in China and has emerged as a new structural approach in recent years. This paper presents a case study on large shaking table tests that explore various seismic responses of a pile group system based on the Kunming South Railway Station. The study focused on the dynamic characteristics of both the soil and the pile-superstructure interaction. Findings indicate that pile damage is concentrated on the side facing the direction of vibration, with the middle pile experiencing greater damage than the corner pile. Hysteresis is observed in the growth of the pore pressure ratio during soil liquefaction in saturated conditions. Both the bending moment and the ground pressure acting on the pile increase with the degree of liquefaction. The maximum pile bending moment occurs at the interface between liquefied and non-liquefied soil layers. During seismic events, the side piles facing the vibration direction experience increased seismic surcharge, while the central piles are subjected to lower loads due to the isolation effect of the side piles.

Keywords

Integrated building-bridge structure system, Kunming south railway, Shaking table experiments, Piles, Dynamic response

1. Introduction

The integrated building-bridge structure system, as depicted in Figure 1, represents a typical example of integrated railway stations in China and has emerged as a novel approach in recent years. This new structural system effectively eliminates vibration-induced resonance between the two structures by integrating the station building and the elevated bridge into a single structure, in contrast to traditional train stations. It offers several advantages, such as land-saving for development and providing passengers with direct interchange. This system combines the bridge and the station structure, altering their load transfer mechanisms and dynamic characteristics. (Zhang et al., 2020; Guo et al., 2012; Yang et al., 2013; Yang et al., 2016). Under earthquake conditions, the lower pile foundations are subjected to significant axial and lateral forces due to dynamic soil-structure interaction, especially in areas with liquefiable soils. The seismic forces acting on the pile group can cause substantial bending, shear forces, and axial deformations, which may significantly affect the stability of the structure. These effects are exacerbated by soil liquefaction, which alters the load-bearing capacity of the foundation and increases the likelihood of failure.

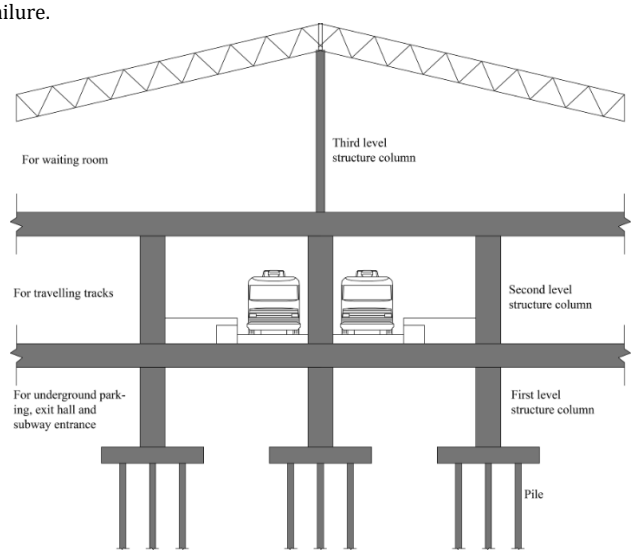

Fig. 1 Integrated building-bridge structure system

Pile foundations are commonly used in heavily loaded structures like buildings, bridges, and ports to support the superstructure. In this system, pile groups are often used to ensure the stability of the superstructure (Fan et al., 1991; Zhang et al., 2016; Sheil & McCabe, 2016; Zhang et al., 2014; Tang et al., 2014). Group piles have significant capacity to withstand static loads, and the pile-soil interaction differs from the interaction of a single pile under seismic loading. Many researchers have used experiments and numerical simulations to investigate seismic soil-pile interaction, particularly in liquefiable soils (Hussein et al., 2021; Dou et al., 2024; Zhang et al., 2020). These studies provide valuable insights into the fundamental behavior and damage mechanisms of pile-supported structures in different environments, allowing for a deeper understanding of soil-pile structure damage under seismic stress and characterizing the complex dynamic response of piles.

Sandra Escoffier (Escoffier, 2012) studied the influence of inclined piles on the seismic response of pile groups by comparing the seismic responses of two groups of simplified piles in centrifuge tests. Fayun Liang (Liang et al., 2020) conducted a series of seismic centrifuge tests on an RC girder-type bridge with a 3 × 3 pile-group foundation embedded in dry sand to investigate the seismic behavior under different scour conditions. Xiaoyu Zhang (Zhang et al., 2020) studied the damage mechanism of end-bearing piles partially embedded in a saturated sandy soil layer using shaking table tests. The vibration characteristics and damage mechanisms of single piles and pile groups in both liquefied and non-liquefied soils have been studied through numerical simulations and theoretical analysis (Cubrinovski et al., 2017; Cubrinovski et al., 2014; Elsawy et al., 2019; Blanco et al., 2019).

The seismic capacity of pile group foundations is shown to be reduced due to the effect of pile groups, which reduces the resistance of the surrounding soil to the pile. The vibration characteristics of the group piles become a key consideration for Kunming South Station (the project on which this article is based). This study optimizes experimental conditions to better capture the complex interactions between pile foundations and liquefiable soil layers. Additionally, it employs multiscale and multifactor analysis to explore the combined effects of seismic frequency and multidirectional shaking on pile behavior. These advancements ensure that the findings are directly applicable to engineering practice, particularly in addressing the long-term seismic response of pile foundations in liquefiable soils, thereby offering new perspectives for enhancing the reliability and scientific rigor of pile design in seismic regions.

2. Project Overview

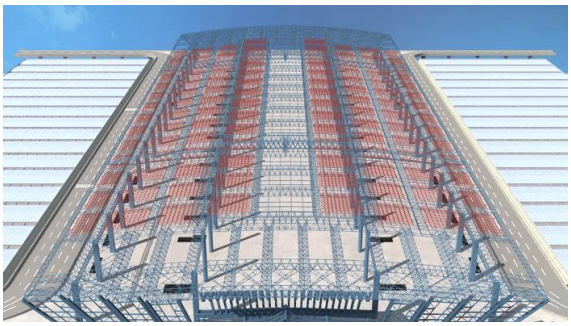

(a) 3D model of the main structure

(b) Scaled model of the station

Fig. 2 Kunming South Railway Station

Table 1. Pile Structure Dimensions

Number	Pile Length/m	Pile Diameter/m	Pile Cap: Length × Width × Height/m	Pier: Length × Width × Height/m
CT3	30	1	5.308×4.598×2.6	1.75×1.75×20
CT5	30	1	6.3×6.3×2.3	2.6×2.0×20
CT9	30	1.2	9.6×9.45×4.3	4.8×1.8×20

Kunming South Railway Station, as shown in Figure 2, is a large high-speed railway station building that adopts the integrated building-bridge structure system. The station has a total construction area of 334,736.5 m^2, including four station yards, 16 platforms, and 30 tracks. The station building is 238 m long (north to south) and 430.5 m wide (east to west), with three above-ground floors and one underground floor. The first level, located underground, has a ground elevation of -10.5 m and is primarily used for underground parking, an exit hall, and a subway entrance. The second level is the platform level, with a platform level at an elevation of 0.0 m, and the third level (elevation 9.5 m) is an elevated waiting room.

Kunming South Railway Station is located in a region with a seismic intensity of 8 degrees, indicating a high earthquake risk. The design includes a horizontal seismic impact coefficient of 0.16, which defines the level of seismic force the structure must withstand. It is also designed to resist a seismic acceleration of 0.2g, representing the maximum ground shaking the station can endure. The site has a characteristic period of 0.45 seconds, which is crucial for understanding how the ground responds to seismic waves and ensuring the foundation's stability during earthquakes. The pile foundation passes through the clay layer, saturated fine sand layer, and pebble layer from top to bottom, and the fine sand layer around the pile foundation exhibits distinct characteristics of vibration-induced liquefaction.

The dimensional parameters of the three commonly used types of C40 reinforced concrete pile structures at Kunming South Station are detailed in Table 1.

3. Description of shaking table test

3.1 Similarity ratio of test

By Buckingham π theorem, using E, σ and L as the fundamental physical quantities and deriving the other physical quantities: $\frac{\lambda_E}{\lambda_a}\lambda_\rho = \lambda_l$, $\frac{l_m}{l_p} = \lambda_l$ Where λ_E、λ_a、λ_ρ、λ_l、l_m、l_p are the modulus of elasticity similarity ratio, acceleration similarity ratio, mass density similarity ratio, and geometric similarity ratio, representing the model and the prototype, respectively. According to the size of the model box and the actual size of the structure, the geometric similarity ratio λL=1/20, the elastic modulus similarity ratio λE=1/5 and the density similarity ratio λρ=2, the acceleration similarity ratio λa=2. Other similar relationships can be calculated by the formula and are not repeated in the text.

Shaking table tests on the pile foundations were carried out using a large 4m × 4m geotechnical shaking table at the School of Construction Engineering, Kunming University of Science and Technology. The shaking table is equipped with a high-performance static-pressure bearing actuator (model 080-160-100P/SAB) manufactured by SERVOTEST Testing Systems Ltd. This actuator provides precise vertical motion capabilities, enabling the simulation of a wide range of seismic conditions. The operating parameters of the shaking table are provided in Table 2.

Table 2. Performance parameters of the shaking table

Table-top size	4m×4m
Maximum load	30t
Maximum acceleration	±1g（20t），±0.8g（30t）
Maximum speed	±0.8 m/s
Maximum stroke	±125mm
The range of operating frequency	0.1Hz～100Hz

The soil container dimensions of 2.2m × 1.5m × 2.2m and a wall thickness of 10mm were selected to ensure proper scale for the shaking table tests while maintaining structural integrity. The 10 cm thick foam sheets are employed to reduce boundary effects, minimize reflections during shaking table tests, and ensure accurate simulation of soil-structure interaction. Additionally, they help maintain structural stability within the model box and prevent soil or water seepage, ensuring the integrity of the liquefaction conditions.

These dimensions provide adequate space for the soil layers, pile foundations, and superstructure model, ensuring realistic simulation of soil-structure interaction. The 10mm thickness ensures the container can withstand the dynamic forces of the tests without deforming, while also minimizing boundary effects that could skew results. Additionally, the inner foam lining further reduces the impact of boundary reflections, enhancing test accuracy. During the dynamic test, the container boundary applies a binding force on the soil. The deformation limitation from the container boundary, along with the reflection and changes in the vibration pattern of the structural system, may introduce errors in the test results. To simulate actual site conditions more accurately, the boundary conditions of the model box were processed to reduce the influence of the boundary on the test results. The inner wall of the model box was wrapped in 10 cm thick foam sheets for the test. To prevent the foam from floating off the inner wall of the model box during the test, the contact surface between the foam and the inner wall was glued using silica gel. The foam also acted as an impermeable barrier. The model box is shown in Figure 3, with the internal foam shown in Figure 4.

Fig. 3 Model box

Fig. 4 Internal foam

3.2 The model soil-piles-superstructure system

The soil in the model box is divided into three layers: the lower part is a dense sand layer (0.5 m), the middle is a saturated sand layer (1.3 m), and the upper part is a clay layer (0.3 m). First, the bottom sand is placed into the model box, then the sand is evenly tamped, and the relative density of the dense sand layer was checked to ensure it met the requirements. After placing the bottom dense sand layer, the model box was partially filled with water to a predetermined height. The sand is poured into the model box from a constant height until the sand layer reaches a pre-specified height to ensure uniformity. The model clay layer was placed on top of the sand layer when it reached the final height, and the water level on the surface of the clay layer was maintained. It is important to note that the relative density of the saturated sand layer is difficult to measure directly and is estimated to be around 60%, based on previous water sink method tests (Xu et al., 2020).

The sandy soil of Kunming South Station was selected as the liquefiable soil and the clay as the non-liquefied layer of the overlying soil. Based on the grading curve, d10=0.20, d30=0.355, d50=0.511, d60=0.619, non-uniformity coefficient $C_u = \frac{d_{60}}{d_{10}} = 3.095$, coefficient of curvature $C_c = \frac{(d_{30})^2}{d_{60} \times d_{10}} = 1.02$. The grain size distribution indicated a predominance of sand, with minor fractions of silt and clay, as determined by sieve analysis. The dry density of the soil was measured as 1.52 g/cm^3. The plasticity index was determined based on Atterberg limits, with a liquid limit of 20.1% and a plastic limit of 5.4%. The shear strength parameters, including cohesion (c = 3 kPa) and the angle of internal friction (φ = 22°), were obtained through triaxial shear tests.

The test structure consists of piles, a pile cap and a superstructure mass block. The test model design is based on the typical pile foundation of Kunming South Station, which uses C40 reinforced concrete foundation piles. The pile group consists of nine piles, each with a length of 30 m and a diameter of 1.2 m. The size of the pile cap is 9.6 m × 9.45 m × 8.3 m. The size parameters of the test prototype designed according to the above similarity ratio are shown in Table 3. The height of the model pier is 1m, the height of the pier is 0.55m, and the height of the column pier is 0.45m.

Table 3. Structural dimensions of prototype pile and model pile

Type	Pile Length /m	Pile Diameter /m	Pile Cap: Length × Width × Height /m	Pier: Length × Width × Height /m
Prototype pile	30	1.2	9.6×9.45×4.3	4.8×1.8×20
Model pile	1.5	0.060	0.480×0.472×0.215	0.240×0.900×1.000

The mass block of the superstructure is calculated using the equivalent density similarity ratio, based on the model parameters. The model dimensions are shown in Figure 5.

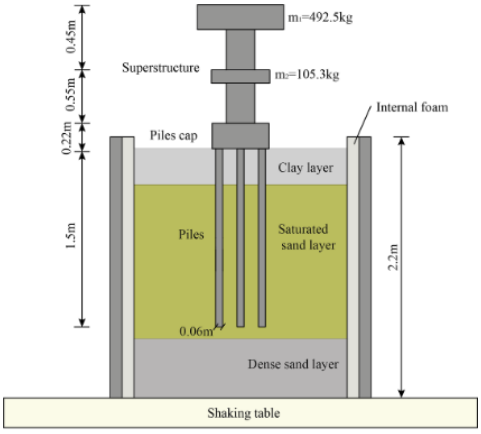

(a) Front view

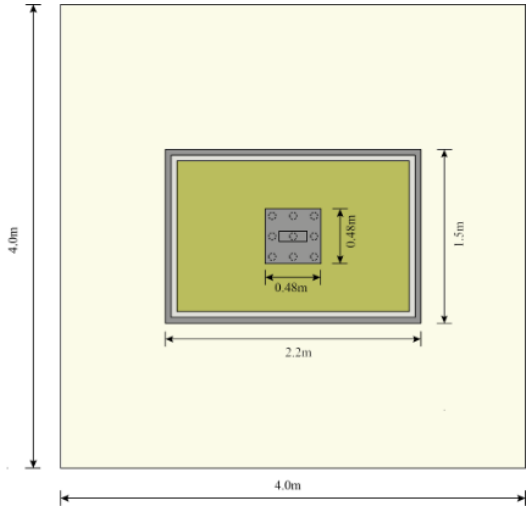

(b) Top view

Fig. 5 The model and model dimensions

The mass block of the superstructure is calculated as follows:

The equivalent density similarity ratio is defined in Equation 1:

$$\lambda_d = (m_m + m_{om} + m_a)/\lambda_l^3(m_p + m_{op}) \quad (1)$$

Where: mm-mass of model members; mom-mass of live load and non-structural members in the model; ma-artificial mass imposed by the model structure; mp-mass of prototype structural members; mop-mass of live load and non-structural members in the prototype structure.

If the model live load and the mass of non-structural members are neglected (mop=0), it is obtained from equation (1).

$$m_a = \lambda_d \lambda_l^3 m_p - m_m \quad (2)$$

According to the dimensional relationship between the modulus of elasticity and the mass density:

$$\lambda_d \lambda_l^3 = \lambda_E \lambda_l^2 \quad (3)$$

Artificial mass to be applied to the model superstructure:

$$m_a = \lambda_E \lambda_l^2 m_p - m_m \quad (4)$$

The piles, pile cap, and superstructure are cast in one piece. The piles are made of particulate concrete and 10# galvanized iron wire (diameter: 3.50 mm), and the pile cap and the superstructure are made of concrete and steel (diameter: 6 mm). To ensure reliability and reproducibility of the results, three specimens were cast. Each specimen underwent independent testing, and the average values of compressive strength and elastic modulus were reported to ensure the accuracy of the experimental data. The particulate concrete mixture proportions for the piles were: cement: fine aggregate: coarse aggregate: water in the ratio of 1:8.3:3.0:1.2. Aggregates with particle size of 2.5 mm–5.0 mm replace the crushed stone in the prototype concrete, and river sand with a particle size of less than 2.5 mm and continuous grading, which replaces the fine aggregate of the prototype concrete, with a fineness modulus of 1.91 and mud content of 8.2%; 42.5-grade silicate cement is used; potable water is used for mixing. The average compressive strength of the piles was determined to be 15.5 MPa. This value was measured using cube testing conducted in accordance with China standards, which specify procedures for determining the compressive strength of concrete specimens. The tests were carried out on 150 mm × 150 mm × 150 mm cubes prepared from the same concrete batch as the piles and cured for 28 days under standard conditions (23°C ± 2°C, >95% relative humidity). The average elastic modulus of 13.2 GPa was derived from uniaxial compression tests performed on cylindrical specimens (100 mm diameter × 200 mm height). The tests were carried out using a strain-controlled loading system, ensuring precise measurement of stress-strain relationships. The model fabrication process is shown in Figure 6. The steel boxes shown in Figure 6(b) serve as mass blocks designed to simulate the mass of the superstructure. These blocks are calibrated to replicate the dynamic characteristics and load distribution of the actual upper structure, ensuring that the model accurately represents real-world seismic behavior.

(a) Fabrication of reinforcement cage for piles

(b) Fabrication of reinforcement cage for superstructure

(c) Mould removal and maintenance

Fig. 6 The model making process

The accelerometers are installed in two locations: one is buried in the soil to monitor the variation in soil acceleration during vibration, and the other is installed on the pile cap and the superstructure to monitor the variation in superstructure acceleration. The pore water pressure

transducers are arranged in the saturated sand to monitor the change in pore water pressure in liquefiable sand. Earth pressure boxes are symmetrically placed on both sides of the piles to monitor the change in contact pressure between the pile and the soil during vibration. Fourteen accelerometers, five pore water pressure transducers, 24 earth pressure boxes, and 48 strain gauges were deployed in the test, as shown in Figure 7. The deformation of both the superstructure and the soil is measured by laser displacement sensors. It can accurately and non-contact measure the position and displacement of the structure.

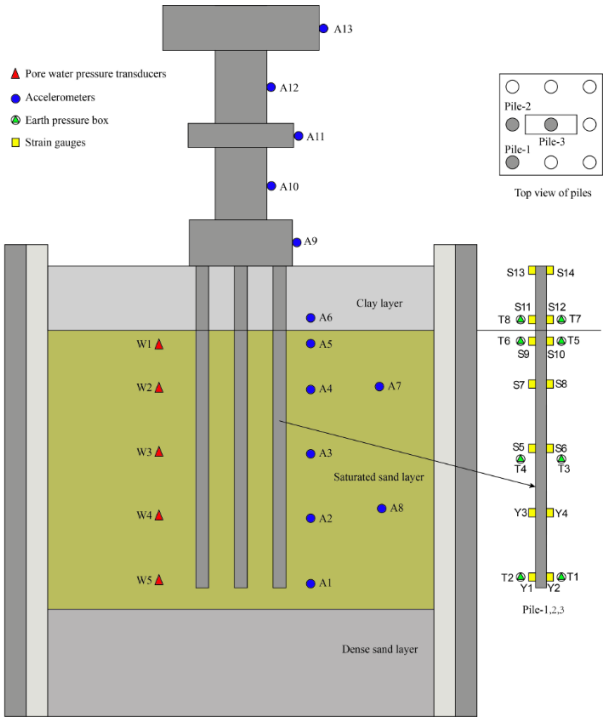

Fig. 7 Monitoring point

3.3 Seismic wave input

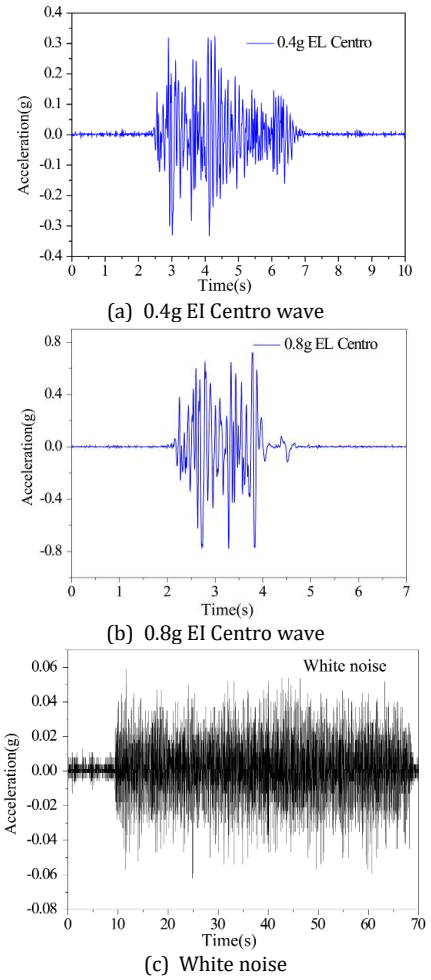

Fig. 8 The time curve of input wave

The fundamental characteristics of the soil–pile–superstructure system was identified using white noise excitation. This analysis provided insights into the system's natural frequency and damping ratio, which are crucial for understanding its seismic response and dynamic properties under varying loading conditions. The EL-Centro wave is selected as the input wave. The amplitude was adjusted according to the specific test loading requirements. The EL-Centro wave is the acceleration time history reported by the IMPERIAL VALLEY EARTHQUAKE (M7.1) in the United States on May 18, 1940, which is typical of ground shaking of magnitude VIII.

In the test, a unidirectional seismic wave loading was applied along the X-axis, simulating ground motion in a single horizontal direction. The input motion was based on El Centro, scaled to match the target peak ground accelerations of 0.4g and 0.8g, representing moderate and strong earthquake intensities, respectively. This approach ensured controlled and consistent seismic input to evaluate the structural response under liquefaction conditions. And modal tests with white noise are performed before and after each level of loading. The original wave is processed by filtering and baseline correction to serve as seismic load input, and the time curve of the input wave is shown in Figure 8.

4. Test results and interpretation

4.1 Experimental macroscopic phenomena

The main macroscopic damage characteristics observed during the test can be verified with the results from the sensor data. Macroscopic phenomena under different seismic input intensities are shown in Table 4. Test sites of the two groups after loading are shown in Figure 9.

Table 4. The macroscopic phenomena of different seismic input intensities

Input	PGA(g)	Piles	Ground surface	Superstructure
EL - Centro wave	0.4	There are a few tiny cracks visible.	A little amount of water seeps from the clay layer, and the saturated sand layer is partially liquefied. The soil is separated from the bottom of the piles cap.	The vibration amplitude increases, and a slight tilt occurs. The superstructure is sunken by 9mm, with a lateral offset of 7mm.
	0.8	The link between the piles and the piles cap has fractured	Puddles formed due to severe liquefaction of the saturated sandy layer and sinking of soil around piles cap.	Significant tilting of the Superstructure. The superstructure is sunken by 35mm, with a lateral offset of 18mm.

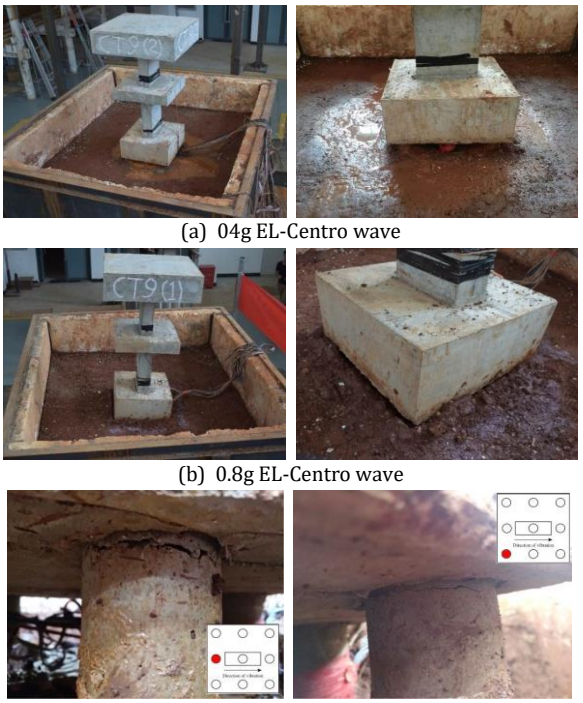

(a) 04g EL-Centro wave

(b) 0.8g EL-Centro wave

(c) The link between the piles and the piles cap has fractured (0.8g)

Fig. 9 The test site of the two groups after loading

4.2 Dynamic characteristics of soil

Figure 10 illustrates the time histories of the excess pore pressure ratios at measurement points W1–W5. Figure 10(a) indicates that the maximum pore pressure ratio is 0.57 at W1 and the minimum is 0.21 at W5 during the 0.4g EL-Centro wave test. Figure 10(b) indicates that the maximum pore pressure ratio is 0.98 at W1 and the minimum is 0.65 at W5 during the 0.8g EL-Centro wave test. Exceeding a pore pressure ratio of 0.8 is considered indicative of liquefaction, as noted by Xu et al. (2020). The saturated sand layer experiences partial liquefaction under a 0.4g EL-Centro wave, while it undergoes severe liquefaction at a 0.8g EL-Centro wave, consistent with the observed macroscopic phenomenon.

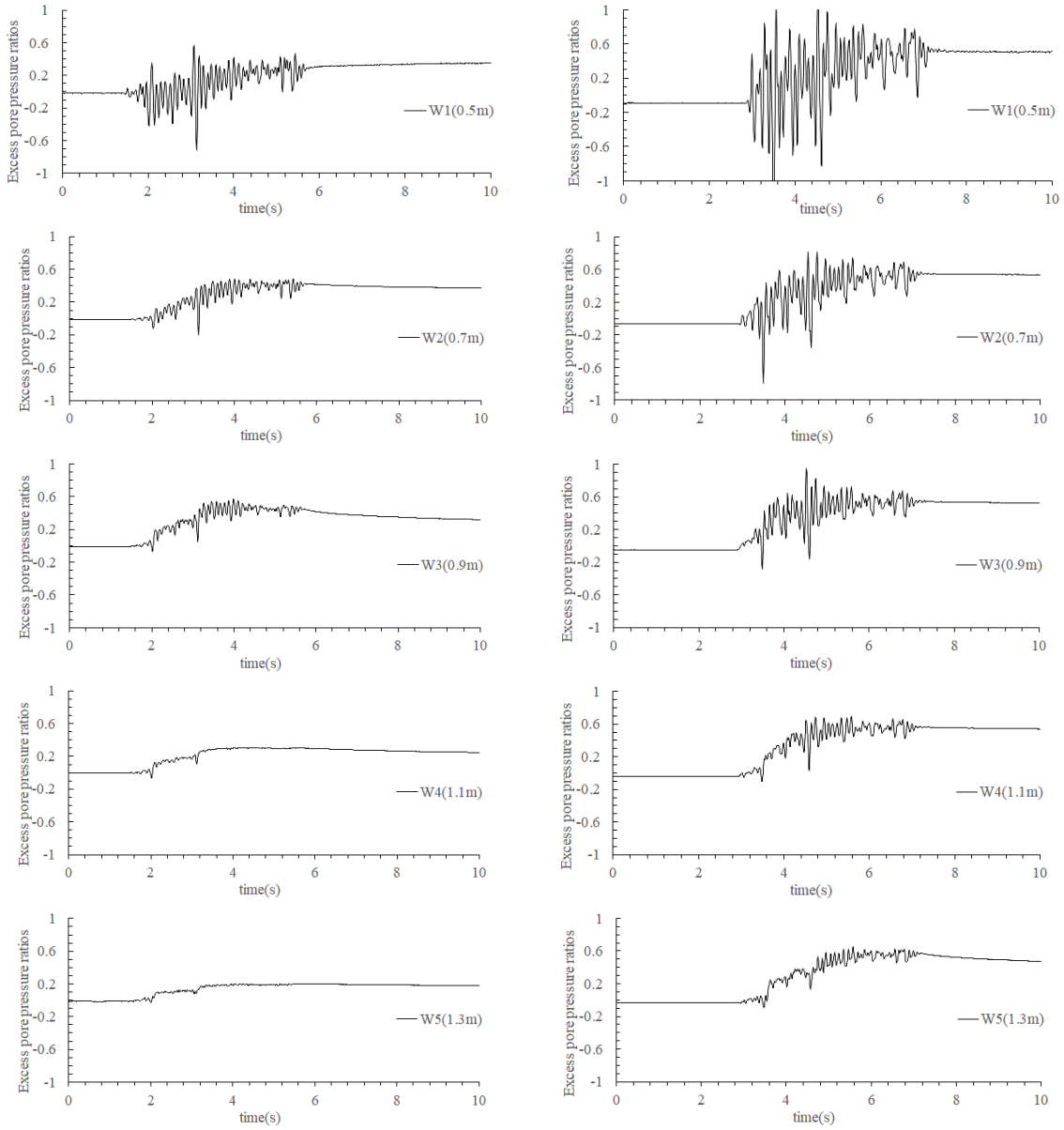

(a) 0.4g EL-Centro wave (b) 0.8 g EL-Centro wave

Fig. 10 The time histories of excess pore pressure ratios

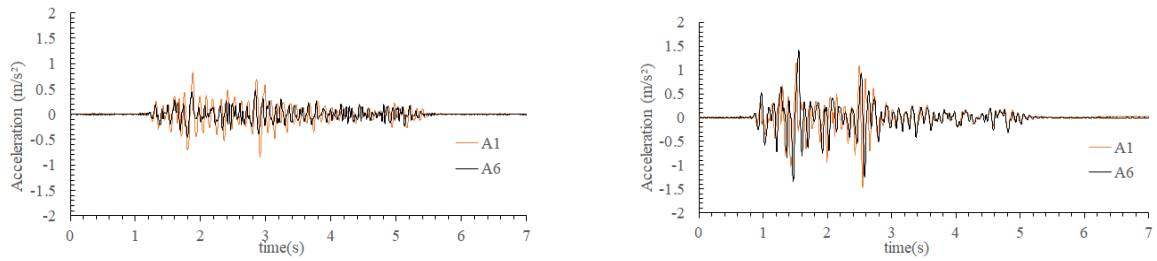

(a) 0.4g EL-Centro wave (b) 0.8 g EL-Centro wave

Fig. 11 The time histories of soil bottom acceleration(A1) and soil surface acceleration(A6)

The time histories of soil bottom acceleration (A1) and soil surface acceleration (A6) under two test conditions are shown in Figure 11. Fig. 11(a) shows a considerable increase in the acceleration pulse amplitude at the ground surface (PGA = 0.4g). The sandy soil used in the model test primarily amplifies seismic waves. However, with PGA = 0.8g, acceleration amplification is not visible at the ground surface. Soil nonlinearity increases when it softens under high-intensity vibration, leading to a decrease in the soil's ability to transmit seismic waves.

4.3 Dynamic characteristics of piles and superstructure

Dynamic amplification factors of the peak acceleration are calculated as the ratio of the response peak to the input peak acceleration. Figure 12 shows the amplification factors of the peak acceleration for the structure in the tests. The variation pattern of the amplification factor of the peak acceleration is basically the same for the two test conditions, first increasing and then decreasing, in an 'S' shape. The amplification factors of the peak acceleration are 1.47 and 1.76, respectively. Both occur at the

top of the structure, indicating that the top of the structure vibrates more strongly when subjected to vibration. In the middle of the pile, the acceleration amplification is strong, and the extreme value occurs in the transition section between the saturated sand layer and the clay layer, where the acceleration amplification coefficient is reduced. This event causes a fracture susceptibility at the link between the pile cap and the pile, which aligns with the damage pattern described in Figure 9(c).

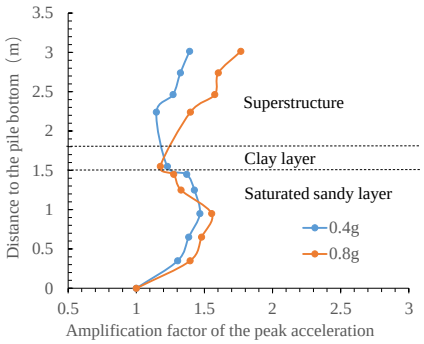

Fig. 12 Amplification factor of the peak acceleration

Figure 12 shows the additional soil pressure acting on piles due to vibration. As seen in Figure 12, the pile-soil contact pressure increases with the increase in earthquake magnitude. The soil pressure in the clay layer is greater than the soil pressure in the saturated sand layer at PGA = 0.4g, with a pattern of higher pressure at the center and lower pressure at both ends along the pile. At PGA = 0.8g, the soil pressure decreases throughout the pile, and the soil pressure in the saturated sandy layer is much higher than the clay contact pressure. This is due to the slight liquefaction of the saturated sand layer when loaded with 0.4g seismic excitation, and the strength of the sandy soil does not change much. When loaded with 0.8g seismic excitation, the saturated sand layer undergoes severe liquefaction, the strength decreases, and the soil enters the plastic state.

According to the Euler-Bernoulli theory, the bending moment of the pile was obtained by calculating the test data using Equation (5).

$$M=\frac{EI(\varepsilon_t-\varepsilon_c)}{2r} \quad (5)$$

where EI is the pile flexural stiffness, assuming the pile is in an elastic state during vibration; $\varepsilon_t - \varepsilon_c$ is the tensile and compressive strains on both sides of the pile; and r is the radius of the pile.

The additional soil pressure caused by vibration is shown in Figure 13. Figure 14 demonstrates that the peak bending moment increases with increasing vibration acceleration. The pile bending moment increases and subsequently drops in a V-shaped pattern. The bending moment near the bottom of the pile is smallest, and the larger bending moment is concentrated in the transition section between the saturated sand and clay layers. Bending moment decay occurs in the clay layer.

The relative motion between the pile and the superstructure is intensified at the seismic level, resulting in a greater bending moment, with the peak bending moment mostly appearing at the soil delamination and the interface between the pile cap and the pile. The minimum pile bending moment occurs at the bottom of the pile, and the larger bending moment is concentrated in the transition section between the saturated sand and clay layers, where bending moment decay occurs in the clay layer.

The seismic level intensifies the relative motion between pile and superstructure, resulting in a larger bending moment, and the peak bending moment mainly appears at the soil delamination and at the interface between pile cap and pile. The seismic performance of these two areas should be considered during the design phase.

Regardless of soil pressure or peak bending moment, the load on the side pile (Pile 2) is greater than that on the corner pile (Pile 1) and the center pile (Pile 3). Under seismic action, the side piles facing the vibration direction are subjected to increased seismic surcharge loads, while the center piles experience smaller seismic surcharge loads due to the isolation effect of the side piles.

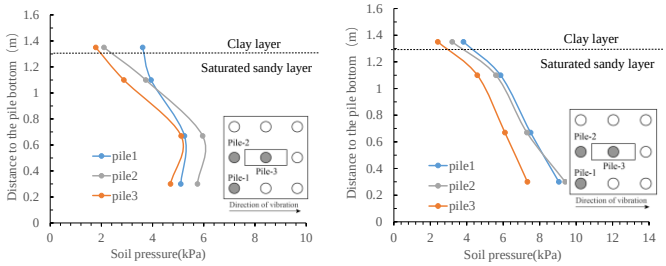

(a) 0.4g EL-Centro wave (b) 0.8 g EL-Centro wave

Fig. 13 Additional soil pressure caused by vibration

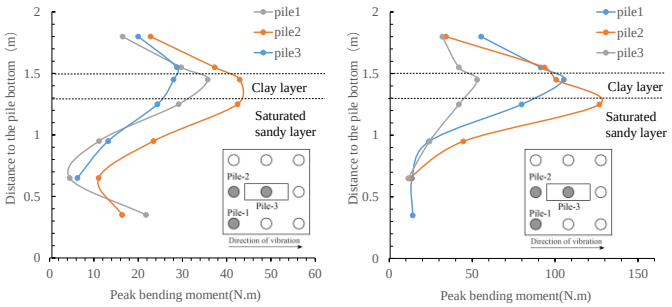

(a) 0.4g EL-Centro wave (b) 0.8 g EL-Centro wave

Fig. 14 The peak bending moment of the pile caused by the vibration

5. Conclusion

This paper presents a case study of large shaking table tests on the seismic responses of a pile group system at Kunming South Railway Station. The study investigates the distinct behaviors of the soil and piles during ground shaking, aiming to provide insights for design and construction. The analysis of test results leads to the following conclusions:

(1) The seismic response of reinforced concrete pile groups in liquefiable soils was investigated through shaking table experiments. The results revealed critical failure mechanisms of pile groups under seismic loading, which included bending failure, buckling failure, and shear failure at the pile head. Bending failure was observed at the interface between liquefied and non-liquefied soil layers due to differential lateral displacements. Buckling failure occurred within the liquefied sand layer as the lateral support diminished, reducing pile stability under axial loads. Additionally, shear failure was concentrated at the pile head due to the rigid pile cap's inability to dissipate dynamic forces. These failure modes were more pronounced under high-intensity seismic loading (PGA = 0.8g), underscoring the significance of considering soil-pile interactions in design.

(2) The dynamic response of the soil-pile-superstructure system varied with seismic intensity. At moderate intensity (PGA = 0.4g), sandy soil amplified seismic waves, resulting in a significant increase in surface acceleration. However, at high intensity (PGA = 0.8g), the soil's nonlinearity caused a reduction in acceleration amplification due to softening and reduced wave transmission. Furthermore, the increase in pore water pressure during shaking confirmed the onset of liquefaction, which was followed by dissipation during the post-seismic recovery phase, highlighting the dynamic characteristics of the soil system under liquefaction conditions.

(3) Bending and buckling failures must be mitigated through design enhancements that account for critical interfaces between soil layers. Shear concentration at the pile head needs to be managed to ensure structural integrity. This study provides valuable insights into the dynamic behavior and failure mechanisms of pile groups, offering practical guidance for engineering applications in seismic regions.

Funding

The authors gratefully acknowledge the support provided by the National Natural Science Foundation of China (Grant No.52108385) and Sichuan Science and Technology Program (2022ZYDF083)

Data Availability Statement

The data presented in this study are available on request from the corresponding author. The data are not publicly available due to the possibility of use in further research.

Conflicts of Interest

The authors declare no conflict of interest.

References

Blanco G., Ye A., Wang X., 2019. Parametric pushover analysis on elevated RC pile-cap foundations for bridges in cohesionless soils. J. Bridge Eng. 24(1), 04018104. https://doi.org/10.1061/(asce)be.1943-5592.0001328

Cubrinovski M., Bray J.D., Torre C.D.L., et al., 2017. Liquefaction effects and associated damages observed at the Wellington Centerport from the

2016 Kaikoura earthquake. Bull. N.Z. Soc. Earthq. Eng. 50(2), 152–173. https://doi.org/10.5459/bnzsee.50.2.152-173

Cubrinovski M., Winkley A., Haskell J., et al., 2014. Spreading-induced damage to short-span bridges in Christchurch, New Zealand. Earthq. Spectra 30(1), 57–83. https://doi.org/10.1193/030513eqs063m

Dou, P., Liu, H., Xu, C., et al., 2024. Numerical analysis on seismic response and failure mechanism of articulated pile–structure system in a liquefiable site from shaking-table experiments. Front. Struct. Civ. Eng., 18(7), 1117-1133. https://doi.org/10.1007/s11709-024-0958-5

Elsawy M.K., El Naggar M.H., Cerato A.B., et al., 2019. Data reduction and dynamic p-y curves of helical piles from large-scale shake table tests. J. Geotech. Geoenviron. Eng., ASCE 145(10), 04019075. https://doi.org/10.1061/(asce)gt.1943-5606.0002146

Escoffier S., 2012. Experimental study of the effect of inclined pile on the seismic behavior of pile group. Soil Dyn. Earthq. Eng. 42(4), 275–291. https://doi.org/10.1016/j.soildyn.2012.06.007

Fan K., Gazetas G., Kaynia A., et al., 1991. Kinematic seismic response of single piles and pile groups. J. Geotech. Eng. 117(12), 1860–1879. https://doi.org/10.1061/(asce)0733-9410(1991)117:12(1860)

Guo W., Yu Z., Zhang H.S., 2012. Application of Story Isolation Technique in the Seismic Reduction of Integrated Building-Bridge Station. In: Sustainable Transportation Systems: Plan, Design, Build, Manage, and Maintain, pp. 464–472. https://doi.org/10.1061/9780784412299.0056

He Z., Ye A., 2014. Influence of group effect on the seismic performance of elevated pile-cap foundation in sand. China Civ. Eng. J. 47(1), 10. https://doi.org/10.1061/(asce)be.1943-5592.0000797

Hussein, A.F., El Naggar, M.H., 2021. Seismic axial behaviour of pile groups in non-liquefiable and liquefiable soils. Soil Dyn. Earthq. Eng., 149, 106853. https://doi.org/10.1016/j.soildyn.2021.106853

Liang F., Liang X., Zhang H., et al., 2020. Seismic response from centrifuge model tests of a scoured bridge with a pile-group foundation. J. Bridge Eng. 25(8), 04020054. https://doi.org/10.1061/(asce)be.1943-5592.0001594

Sheil B.B., McCabe B.A., 2016. An analytical approach for the prediction of single pile and pile group behaviour in clay. Comput. Geotech. 75, 145–158. https://doi.org/10.1016/j.compgeo.2016.08.031

Tang L., Ling X., 2014. Response of an RC pile group in liquefiable soil: A shake-table investigation. Soil Dyn. Earthq. Eng. 67(Dec.), 301–315. https://doi.org/10.1016/j.soildyn.2014.10.015

Xu C., Dou P., Du X., et al., 2020. Seismic performance of pile group-structure system in liquefiable and non-liquefiable soil from large-scale shake table tests. Soil Dyn. Earthq. Eng. 138, 106299. https://doi.org/10.1016/j.soildyn.2020.106299

Yang N., Liu Z., Guo T., et al., 2013. Field measurement and analysis of train-induced vibration of "building-bridge integration" structure. Zhongguo Tiedao Kexue 34(2), 29–35. (in Chinese)

Yang Y., Li Q.S., Yan B.W., 2016. Specifications and applications of the technical code for monitoring of building and bridge structures in China. Adv. Mech. Eng. 9(1), 1687814016684272. https://doi.org/10.1177/1687814016684272

Zhang, H., Qian, D., Shen, C., et al., 2020. Experimental investigation on the dynamic response of pile group foundation on liquefiable ground subjected to horizontal and vertical earthquake excitations. Rock Soil Mech., 41(3), 6. https://rocksoilmech.researchcommons.org/journal/vol41/iss3/6/10.16285/j.rsm.2019.5306

Zhang Q., Liu S., Zhang S., et al., 2016. Simplified non-linear approaches for response of a single pile and pile groups considering progressive deformation of pile-soil system. Soils Found. 56(3), 473–484. https://doi.org/10.1016/j.sandf.2016.04.013

Zhang Q.Q., Li S.C., Liang F.Y., et al., 2014. Simplified method for settlement prediction of single pile and pile group using a hyperbolic model. Int. J. Civ. Eng. 12(2), 146–159.

Zhang X., Ruan L., Zhao Y., et al., 2020. A frequency domain model for analysing vibrations in large-scale integrated building–bridge structures induced by running trains. Proc. Inst. Mech. Eng. F J. Rail Rapid Transit 234(2), 226–241. https://doi.org/10.1177/0954409719841793

Zhang X., Tang L., Li X., et al., 2020. Effect of the combined action of lateral load and axial load on the pile instability in liquefiable soils. Eng. Struct. 205, 110074. https://doi.org/10.1016/j.engstruct.2019.110074

Disclaimer